Unilamellar vesicle formation and encapsulation by microfluidic jetting

Jeanne C. Stachowiak*, David L. Richmond†, Thomas H. Li*, Allen P. Liu†, Sapun H. Parekh‡, and Daniel A. Fletcher†‡§

*Department of Mechanical Engineering, †Biophysics Graduate Group, and ‡Department of Bioengineering, University of California, Berkeley, CA 94720

Compartmentalization of biomolecules within lipid membranes is a fundamental requirement of living systems and an essential feature of many pharmaceutical therapies. However, applications of membrane-enclosed solutions of proteins, DNA, and other biologically active compounds have been limited by the difficulty of forming unilamellar vesicles with controlled contents in a repeatable manner. Here, we demonstrate a method for simultaneously creating and loading giant unilamellar vesicles (GUVs) using a pulsed microfluidic jet. Akin to blowing a bubble, the microfluidic jet deforms a planar lipid bilayer into a vesicle that is filled with solution from the jet and separates from the planar bilayer. In contrast with existing techniques, our method rapidly generates multiple monodisperse, unilamellar vesicles containing solutions of unrestricted composition and molecular weight. Using the microfluidic jetting technique, we demonstrate repeatable encapsulation of 500-nm particles into GUVs and show that functional pore proteins can be incorporated into the vesicle membrane to mediate transport. The ability of microfluidic jetting to controllably encapsulate solutions inside of GUVs creates new opportunities for the study and use of compartmentalized biomolecular systems in science, industry, and medicine.

vortex | liposome | drug delivery | synthetic biology

Encapsulation of enzymes in lipid vesicles was first attempted by Sessa and Weissmann in 1970 (1). Since then, vesicles encapsulating biologically active compounds have been used as chemical microreactors (2), delivery vehicles for pharmaceuticals (3), and platforms for synthetic biological systems (4, 5). Because mixtures of lipids and biomolecules will not spontaneously organize into solution-encapsulating vesicles of defined composition and size, several methods have been devised to form and load vesicles including swelling (6), extrusion (7), electroformation (8), electroinjection (9), and reverse evaporation and emulsion (10, 11).

Among the most important properties of a vesicle formation and loading technique are control of (*i*) membrane unilamellarity, (*ii*) vesicle size, and (*iii*) internal solution concentration without solute-specific selectivity. Furthermore, practical applications of vesicle encapsulation require high encapsulation efficiency to minimize needed solution volume, high-throughput formation, and the ability to examine the vesicle and any associated reactions immediately after loading. Furthermore, In applications to study *in vitro* protein assemblies (12) and cell-like membrane deformations (13), giant unilamellar vesicles (GUVs) with diameters >10 μm are desirable to facilitate direct visualization of internal behavior by light microscopy.

Although each existing vesicle-formation technique achieves some of these criteria, none enables vesicle formation and encapsulation with all of these properties. For example, swelling typically results in the formation of multilamellar vesicles (MLVs) that vary widely in size and encapsulate with low, solute-specific efficiency (2). Electroformation can produce GUVs with diameters >10 μm. However, vesicle diameter is not controlled, and the technique is restricted to low-ionic-strength conditions, limiting its applicability for encapsulation of biomol-

ecules (14). The size uniformity of GUVs and the unilamellarity of MLVs made by several techniques (6, 8, 10) can be greatly enhanced by extruding the vesicles through filters with submicrometer pores, although the resulting vesicles are limited to the size of the pores and have the same internal composition as the original vesicles (15). The reverse emulsion technique offers the advantage of solute-independent encapsulation. However, the size of vesicles produced by reverse emulsion is not directly controllable and throughput is limited (16). Recently, several groups have reported the high-throughput production of monodisperse single- and double-emulsion structures using microdevices that hydrodynamically focus fluid streams (17–19) and pulsed microfluidic jets that deform interfaces (20), although none has been shown to form unilamellar vesicles, an essential requirement for many applications.

Here, we demonstrate the formation and loading of GUVs by microfluidic jetting-induced deformation of a planar lipid bilayer (Fig. 1*a*). This technique relies on a precisely controlled pulsatile liquid jet directed into a unilamellar lipid bilayer formed between two aqueous phases (Fig. 1*b*). One GUV is formed for each pulse of the liquid jet against the lipid bilayer, which remains intact after the vesicle is formed, and multiple monodisperse vesicles are formed by repeated pulses against the same lipid bilayer (Fig. 1*c*). Using high-speed video microscopy, we examine the vesicle-formation process to investigate the fluid-membrane interactions that determine vesicle size and enable vesicle separation from the planar bilayer. Finally, we encapsulate a solution of 500-nm-diameter particles and demonstrate protein pore-mediated transport of solutes across vesicle boundaries.

Results and Discussion

Vesicles produced by microfluidic jetting against a planar lipid bilayer are highly uniform in size and robust, outlasting the observation time of several hours after formation. The average vesicle diameter was 208 μm based on a total measured population of 46 GUVs, varying by 2–3% for a given series of pulses and by <7% for different planar bilayers and nozzles of nominally the same size, 40 μm (Fig. 1 *c* and *d*). Multiple vesicles can be created in rapid succession because lipid molecules capable of replenishing the planar bilayer are available in high concentration (in the supporting oil phase around the black film). High-throughput formation of thousands of vesicles per minute is feasible based on a formation time of 5 ms per GUV but was not the objective of this work. Because the vesicle is created from a

BIOPHYSICS

Fig. 1. Formation of GUVs by microfluidic jetting. (*a*) Schematic of the piezoelectric-driven microfluidic jetting device assembled with the planar lipid bilayer chamber. (*b*) Close-up schematic of the vesicle-formation process, highlighting the interaction of a vortex ring structure with the planar lipid bilayer. (*c*) Independent, monodisperse, GUVs resulting from pulsed microfluidic jetting. (Scale bar: 100 μm.) (*d*) Consistency of vesicle diameter over seven separate trials including a total of 46 GUVs. Error bars represent the first standard deviation.

single lipid bilayer (21), we expect only unilamellar vesicles to be formed with this technique. Furthermore, because this technique relies on large (relative to molecular radii) physical deformations of a planar lipid bilayer to simultaneously form vesicles and encapsulate solutes inside of them, we expect that a wide range of solutions can be encapsulated within vesicles without dependence on specific properties of the solutes such as molecular weight or charge.

We examined membrane shape change and fluid loading during vesicle formation using high-speed bright-field microscopy (5,000–10,000 frames per s). Visualization of the fluid flow was enhanced with refraction contrast by loading one solution (typically 200 mM sucrose) into the microfluidic jet and a different solution (typically 200 mM glucose) for the surrounding media [Fig. 2 and supporting information (SI) Movie 1]. The vesicle-formation process can be described in terms of three stages: (*i*) initial membrane protrusion, (*ii*) membrane collapse and encapsulation, and (*iii*) separation of the vesicle from the membrane.

Central to our understanding of initial membrane protrusion (stage *i*) is the formation of a vortex ring, a flow structure created by shear stresses exerted by fluid emerging from the nozzle into the stationary surrounding fluid (22) (Fig. 3 *Inset* and SI Fig. 6). Approximately 500–700 μs after triggering the actuator, a narrow initial protrusion of the membrane is observed (Fig. 2, t1 and t2). This protrusion has an outer diameter of approximately 120 μm and appears to contain a vortex ring structure with a

Fig. 2. Vesicle-formation process. Individual frames taken from a high-speed movie (7,500 fps) of vesicle formation (t1–t8 correspond to 667 μs, 800 μs, 1,067 μs, 1,467 μs, 2,000 μs, 2,267 μs, 3,200 μs, 4,667 μs after the start of actuator expansion). Bright-field contrast is created by jetting a 200 mM sucrose solution into a surrounding solution of 200 mM glucose. (Scale bar: 100 μm.)

diameter of 50 μm, where the ring defining the axis of vortex flow is taken as the ring diameter (compare Fig. 2, t1 and t2, with SI Fig. 6, t1 and t2).

To understand why the protrusion size (120 μm) significantly exceeds the nozzle size (40 μm), we examine the development of the vortex ring structure in our system, which occurs by a combination of convective and diffusive mechanisms (22, 23). Gharib *et al.* (23) have shown that vortex rings initially grow in diameter by enfolding external fluid, a convective process, until a critical stroke-to-diameter ratio of the fluid pulse, approximately 4, is reached, after which the vortex ring "pinches off" from the jet, and the period of rapid increase in ring diameter ceases (24). In our experiments, the stroke-to-diameter ratio is at least 25 (see *Materials and Methods*), greatly exceeding the critical value. Above the critical value, Shusser and Gharib (25) predict a maximum vortex ring diameter of 1.3–1.4 times the
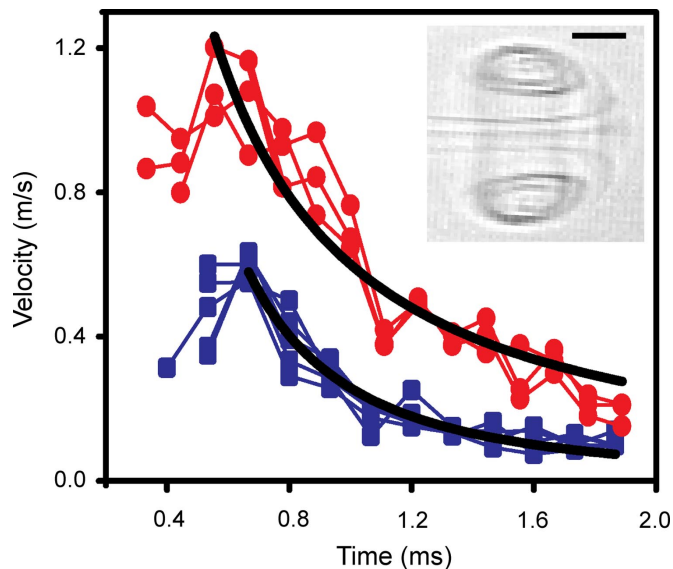
Stachowiak *et al.*

Fig. 3. Kinematics of vortex ring–membrane collision. Decay of vortex ring velocity and membrane protrusion velocity in time. Power law curve fits were applied beginning at the time of maximum velocity. For the vortex (red circles), $V = 0.59t^{-1.26}$ ($R^2 = 0.98$). For the protrusion (blue squares), $V = 0.26t^{-2.00}$ ($R^2 = 0.93$). (*Inset*) Bright-field image of a vortex ring created in the absence of the planar bilayer using an actuator expansion rate equivalent to that used to form GUVs. (Scale bar: 50 μm.)

initial jet diameter from convective growth. This prediction corresponds to an expected vortex ring diameter of 50–60 μm based on the 40-μm nozzle diameter used in our system, in good agreement with the observed value of 50 μm. The Reynolds number, based on initial jet diameter and speed, is approximately 80 (see *Materials and Methods*), justifying the use of this convective analysis.

Vortex rings grow in outer diameter and eventually dissipate by entraining fluid in their vicinity. As fluid is entrained, the momentum of the vortex structure diffuses away from the ring. The length scale of diffusion is of the order $\delta = \sqrt{2vt}$, where v is the fluid kinematic viscosity and t is the time since the vortex began to form (26, 27). At our observation time of 500–700 μs, the expected growth in vortex diameter due to diffusion is then of the order 100 μm. Adding this quantity to the predicted ring size, the expected outer diameter of the vortex structure is of the order 150 μm, consistent with our observed membrane protrusion diameter of 120 μm. This agreement suggests that the diameter of the jet-induced membrane protrusion, which will affect the diameter of the vesicle formed, is strongly influenced by the convective and diffusive growth of the vortex ring structure. Undoubtedly the complex dynamics associated with impingement of the vortex structure on the membrane and the resulting membrane deformation also play an important role in determining the geometry of the membrane protrusion and the size of the resulting vesicle.

Shortly after initial formation, the velocity of an unencumbered vortex ring is expected to decrease inversely with time (22), consistent with our measurement of an unencumbered vortex ring of $v \sim t^{-1.26}$ (Fig. 3, red curve). By comparison, we find for the same actuator expansion rate that the velocity of the starting vortex as it deforms the membrane decreases more quickly with time, as $t^{-2.00}$ (Fig. 3, blue curve), indicating that a significant fraction of the vortex energy is transferred to membrane deformation and reinforcing the importance of the vortex membrane interaction in determining the size of the resulting vesicle.

After formation of the narrow membrane protrusion, fluid continues to fill and expand the protrusion, creating a bolus of

liquid that will become the encapsulated volume of the GUV (Fig. 2, t3). As the liquid jet driving the protrusion slows and ceases, the membrane tension favors contraction while the bolus momentum favors extension (stage *ii*; Fig. 2, t4 and t5). These opposing effects result in the formation of a long, slender membrane neck that eventually arrests further growth of the bolus (Fig. 2, t4 and t5). For actuator expansion rates approximately 10% less than the value used to form vesicles, significant necking was observed, but the membrane failed to form a vesicle and returned to its initial position (SI Fig. 7), indicating that vesicle formation is very sensitive to actuator expansion rate.

During stage *iii*, further elongation and thinning of the membrane neck leads to the formation and extension of a lipid tube (Fig. 2, t6–t8) and ultimately to separation of the newly formed vesicle from the planar bilayer. Forward movement of the bolus as the planar membrane retracts causes the extension of the tube to a length of >1 mm. Although visualization of the membrane tube is difficult with bright-field microscopy, small volumes of fluid (<0.1% of the vesicle volume) trapped along the tube, or pearls, are sometimes observed and, when present, move with the vesicle (SI Fig. 8), confirming the tube's existence. Formation of pearls has been previously observed when membrane tubes are extended dynamically and is attributed to the classic Rayleigh instability (28, 29). This instability occurs when the aspect ratio (length to width) of a column of liquid exceeds the limiting value for stability, approximately π (30). In the case of a two-phase fluid interface such as oil and water, complete collapse leading to droplet formation would result at this point. However, in our case, collapse of the membrane neck is eventually stalled by the bending rigidity of the membrane, which resists the formation of structures with high curvature, leading to the formation of a lipid tube (31). Collapse of the neck into a lipid tube is first observed approximately 2 ms after the start of actuator expansion, when the neck aspect ratio varies from 5 to 10. In all cases, the membrane tube is observed to have disappeared after the vesicle moves away, leaving an intact planar lipid bilayer and a separate, unilamellar, spherical GUV. When the actuator expansion rate is increased significantly beyond that necessary for unilamellar vesicle formation (3–4 times greater), the oil used to support the lipid bilayer is entrained during membrane deformation such that water–oil–water emulsions, rather than unilamellar vesicles, are formed (see SI Figs. 9 and 10 and *SI Text*). These emulsions, which have been observed previously (20), often burst after several minutes (data not shown).

Having examined the vesicle-formation process, we considered several basic properties of our encapsulation technique that are relevant to scientific, industrial, and medical applications. These properties include control of encapsulated concentration, membrane permeability, size-specific solute selectivity of the encapsulation process, and strategies for controlled variation of vesicle size. Control of the concentration of encapsulated solutes is desirable for many applications. Encapsulated concentrations in our system depend on the way in which the experiment is configured. In all configurations, fluid from the side of the planar bilayer opposite the nozzle is kept from entering the vesicle because, as described above, the membrane remains intact throughout the vesicle-formation process. In the case that the solution in the nozzle of the jet is the same as the solution residing on the jet side of the planar bilayer (approximately 30 μl of solution), no solute dilution should occur during encapsulation. If the jetted solution differs from the solution on the jet side of the planar bilayer, the configuration using the smallest amount of encapsulation solution (approximately 1-μl nozzle volume), vesicles will contain a mixture of the two fluids, which can be useful for bioreactor applications in which components are suddenly mixed. The vortex ring formed by the pulsed jet flow will entrain surrounding fluid as it forms and propagates in
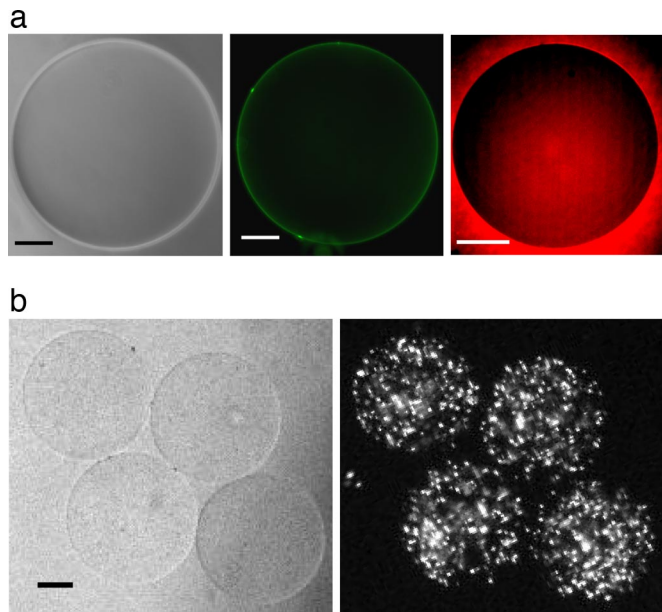
Fig. 4. Characterization of GUVs formed by microfluidic jetting. (*a*) Membrane labeling and volume exclusion for the same GUV. (Scale bars: 50 μm.) (*a Left*) Phase contrast image of the GUV. (*a Center*) Labeling of the GUV membrane using BODIPY dye. (*a Right*) Wide-field fluorescence image documenting exclusion of sulforhodamine B dye by the GUV. (*b*) Encapsulation of polystyrene beads into GUVs with the microfluidic jet. (*b Left*) Bright-field image of four GUVs created from a single planar bilayer. (*b Right*) Encapsulation of fluorescent beads (500 nm diameter, FITC) in GUVs.

a highly reproducible way. Fully formed vortex rings have been shown to contain 25–40% entrained volume (23), but we expect impingement of the vortex ring on a flexible membrane to reduce entrainment compared with that observed for a freely propagating vortex ring.

To test the transport properties of GUVs formed by microfluidic jetting, we examined the permeability of the vesicle membranes to water by exposing them to a fixed, known osmotic gradient. Vesicles initially contained and were surrounded by a solution of 280 mOsm. After vesicle formation, the osmolarity of the solution was increased to 430 mOsm. Over the 15 min after the increase in osmotic pressure, the vesicle diameter decreased by 16%, in good agreement with the predicted 14% decrease based on an osmolarity balance across the membrane (data not shown). Furthermore, we visualized the vesicle's membrane by labeling the vesicle with 100 nM BODIPY lipid probes, which appeared uniform as expected for a bilayer membrane, and we confirmed membrane impermeability to solutes by demonstrating exclusion of membrane-impermeable sulforhodamine dye (Fig. 4*a*). Because fluid from the jet is directly loaded into the lumen of the vesicle, no selectivity based on the molecular weight of the solutes is expected. We confirmed this property by encapsulating a high concentration of fluorescently labeled 500-nm latex beads into the GUVs (Fig. 4*b*), which exceed the hydrostatic radius of biochemical macromolecules by a few orders of magnitude. Finally, we demonstrated biological transport across the vesicle membrane by insertion of the protein pore α-hemolysin during a dye-exclusion experiment (Fig. 5). Increased relative fluorescence of the internal aqueous volume of the vesicle after addition of α-hemolysin monomer confirmed the functional properties of the unilamellar vesicle and demonstrated the ability to modify the membrane for specific applications.
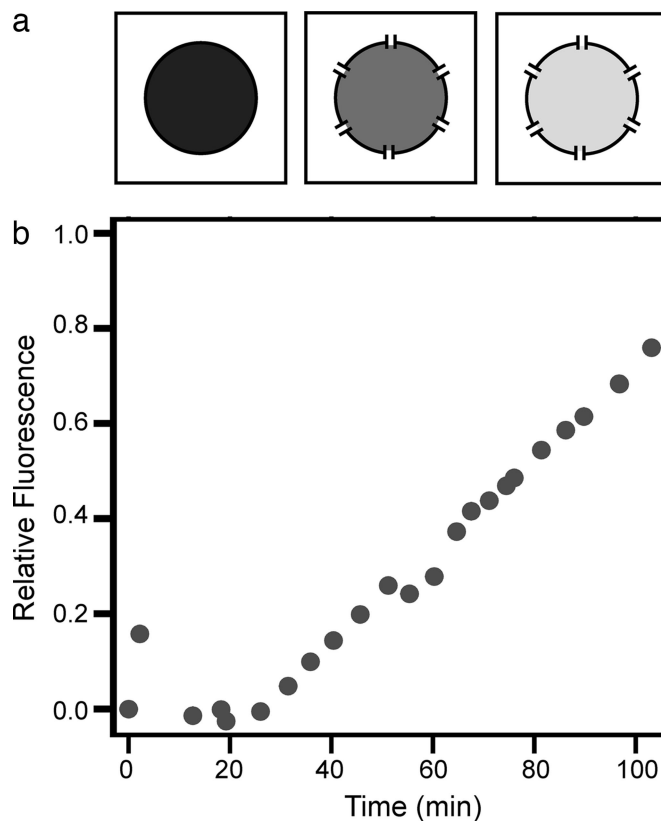

Fig. 5. Protein pore-mediated transport of solutes across vesicle boundaries. (*a*) Schematic diagram. (*b*) Experimental results showing that a GUV initially excluding FITC dye increases in fluorescence relative to the fluorescence of the external solution after addition of α-hemolysin. α-Hemolysin is added to 2.5 μg/ml at time 0, and the vesicle is tracked for 104 min, at which point relative fluorescence has reached 76%.

The formation of vesicles with diameters smaller than those shown in Fig. 1*c* may be desirable for some applications. In the microfluidic jetting technique we describe here, the ability to control vesicle size depends on the capacity for independent control of the pressure and the volume of the expelled fluid pulse. Because growth in vesicle volume is arrested by collapse of the membrane neck to form a lipid tube only after the jet flow slows, control of pulse volume is critical. Additionally, the pressure required to create a narrow membrane protrusion of a given diameter, which is a necessary condition for vesicle formation, increases with decreasing protrusion diameter according to $\delta P \sim \sigma/D$, based on a static force balance, where σ is the membrane tension. In this way, low-volume, high-velocity pulses from small nozzles will produce the smallest vesicles, which, in principle, will have diameters in the range of 1–2 times the nozzle diameter. Using this approach, we have created vesicles close to 100 μm in diameter (data not shown).

For applications in which submicrometer vesicles are required, such as delivery of encapsulated drugs, extrusion of GUVs formed and loaded by microfluidic jetting offers an attractive strategy for formation of liposomes without solution selectivity or dilution of the internal volume (15, 32). Considering bilayer surface area, extrusion of a 200-μm GUV, like those described here, can generate approximately 4 million liposomes of 100 nm diameter. We also note that independent access to both sides of the planar lipid bilayer would provide the ability to specifically modify inner and outer leaflets of the membrane (33).

Here, we have demonstrated a robust technique for unilamellar vesicle formation and encapsulation based on microfluidic

jetting against a planar lipid bilayer. The primary strength of this approach lies in the combination of critical features that it achieves, including unconstrained control of content, unilamellarity, monodispersity of size, the capacity for observation immediately after encapsulation, the formation of large vesicles amenable to observation by conventional microscopy techniques, and the use of small volumes of encapsulated reagent (1–30 μl). The technique also has the clear potential for high encapsulation efficiency (encapsulated volume/jetted volume), control of vesicle size, and high-throughput vesicle production. Although several existing vesicle-encapsulation techniques incorporate some of these features, none has proven suitable for the most challenging biochemical and pharmaceutical applications that require the combination of multiple components to create functional systems capable of interacting with and responding to their environment. The combination of features achieved by the simple microfluidic jetting technique creates new opportunities for forming, studying, and applying multi-component biomolecular systems in fields such as *in vitro* biochemistry, synthetic biology, and pharmaceutical sciences.

Materials and Methods

Solutions Used in the Jet Device. Sucrose and glucose were dissolved in deionized water to achieve the desired concentration and osmolality. Each solution was passed through a 0.2-μm filter. In the experiments to demonstrate encapsulation of particles, a polychromatic red latex microsphere solution (0.5-μm diameter, 2.63% solids; Polysciences) was added in a volume ratio of 3:1,000 after filtration.

Planar Bilayer Formation. Planar lipid bilayers were formed by contacting monolayers as described by Funakoshi *et al.* (20, 34). Bilayer formation took place in a home-built transparent acrylic chamber. The chamber was constructed by laser-cutting an ''infinity'' shape out of a 3-mm-thick sheet of acrylic (TAP Plastics) (Fig. 1 *a* and *b*), where the waist of the pattern was ≈1.5–2 mm wide. A hole of ≈1.4 mm diameter was drilled in one end of the chamber to facilitate the insertion of the glass micronozzle. The chamber was then bonded to a flat, 2-mm-thick, acrylic substrate by using acrylic cement (TAP Plastics). The chamber assembly was allowed to set for at least 8 h at room temperature before use. 1,2-Diphytanoyl-*sn*-glycero-3-phosphocholine (DPhPC; Avanti Polar Lipids) was the lipid used to form the planar bilayers, although the technique need not be specific to this lipid. The lipid was dried under rough vacuum in a test tube for ≈90 min, leaving a dry lipid film on the test-tube walls. After vacuum treatment, the lipid was resuspended in *n*-decane (Sigma–Aldrich) at 25 mg/ml. After addition of *n*-decane, the solution was stored at −20°C with drierite (Drierite). To prepare the planar bilayer, 12–14 μl of the lipid/decane solution was injected into the bottom of the chamber. Water droplets, 27–30 μl in volume, were injected into each side of the chamber sequentially. After formation, the bilayer was allowed to equilibrate for ≈1 min before insertion of the glass micronozzle.

Vesicle Characterization. Vesicles formed by microfluidic jetting were fluorescently labeled with BODIPY 500/510 C$_8$, C$_5$ (Molecular Probes) and tested for exclusion of membrane-impermeable sulforhodamine B (Sigma–Aldrich). To test for functional insertion of a transmembrane protein, we tested incorporation of α-hemolysin into a vesicle. Ten micromolar FITC dye (Molecular Probes) was added to the solution surrounding a vesicle formed by microfluidic jetting, and wide-field fluorescence imaging confirmed exclusion of the dye from the vesicle's internal volume. Next, α-hemolysin monomers (Sigma–Aldrich) were added to the solution surrounding the vesicle to a final concentration of 2.5 μg/ml, and the average fluorescence over a fixed area of the vesicle's internal volume and a fixed area of the external solution were monitored for 104 min. Relative fluorescence of the internal area vs. the

external area was calculated, background-subtracted, and normalized to the total range available for fluorescence to increase inside of the vesicle.

Glass Micronozzle Fabrication. Glass capillary tubing of 1 mm outer diameter and 0.5 mm inner diameter (Sutter Instruments) was pulled to form micropipettes with sharp tips by using a P-97 Flaming/Brown micropipette puller (Sutter Instruments). The tip of the micropipette was further refined by using a Microforge MFG-3 (MicroData Instrument) and sanded to the desired inner diameter of 40 μm. The outer diameter of the finished micronozzle was ≈60–100 μm.

Piezoelectric Jet Device. A piezoelectric actuator rated for 13.9-μm expansion at 120 V (Thorlabs) pushed the plunger of a conventional syringe fitted with a glass micronozzle to produce and control a fluid jet (35). A glass syringe of 343 μm plunger diameter and 2.5 μl metered volume (Model 62) was purchased from Hamilton. The constant rate of actuator expansion was controlled by using custom software written with the program LabVIEW and a 7830R field-programmable gate array card (National Instruments). During vesicle formation, the voltage pulse applied to the piezoelectric actuator was a triangle wave starting from 0 V with a slope of ≈320 kV/s and a maximum value of 120 V. At the low-voltage slew rates used here, the actuator is expected to expand linearly with applied voltage, such that the expected velocity of the expanding actuator is ≈37 mm/s. Using the ratio of plunger to nozzle areas, the maximum possible jet velocity is then ≈2.7 m/s. However, the actual jet velocity was likely somewhat lower due to loss mechanisms such as system compressibility, friction, and flow of fluid around the plunger. Although the jet velocity at the nozzle exit was not directly measured, the velocity of the free vortex ring exiting the nozzle was estimated from our high-speed movies of the ring's evolution in time (SI Fig. 6) and is reported in Fig. 3. Here, the maximum observed vortex ring velocity was ≈1.1 m/s. The theory of vortex ring growth described above predicts a maximum value of ≈1.7 (25) for the ratio of jet to vortex velocity when the stroke-to-diameter ratio of the fluid pulse exceeds the limiting value of 4. In our case, the stroke-to-diameter ratio (where the stroke is taken as the actuator expansion distance multiplied by the ratio of the plunger area to the nozzle area) was >25. Therefore, we estimated the maximum jet velocity at the nozzle exit to be ≈2 m/s. Based on this estimate of jet velocity, and the 40-μm nozzle diameter, the initial Reynolds number at the nozzle exit was approximately 80.

Imaging. High-speed imaging (5,000–10,000 fps) was performed in bright-field on an Axiovert 200 (Zeiss) microscope, using a Photron 1024 PCI monochrome camera. Fluorescent imaging was performed on the Axiovert 200 microscope with a Retiga cooled CCD camera (QImaging) as well as on an AxioObserver (Zeiss) microscope with a CoolSNAP cooled CCD camera (Roper Scientific).

Estimation of Protrusion and Vortex Velocity. The translational velocity of the free vortex ring and the expansion rate of the membrane protrusion were estimated from measurements of the position of the vortex ring and the leading edge of the protrusion, respectively, in high-speed movie frames. The net motion occurring between frames was calculated and divided by the interframe time to estimate velocities.

1. Sessa G, Weissman G (1970) Incorporation of lysozyme into liposomes—A model for structure-linked latency. *J Biol Chem* 245:3295–3301.
2. Walde P (1996) Enzymatic reactions in liposomes. *Curr Opin Colloid Interface Sci* 1:638–644.
3. Lasic DD, Papahadjopoulos D (1995) Liposomes revisited. *Science* 267:1275–1276.
4. Chen IA, Roberts RW, Szostak JW (2004) The emergence of competition between model protocells. *Science* 305:1474–1476.
5. Hanczyc MM, Fujikawa SM, Szostak JW (2003) Experimental models of primitive cellular compartments: Encapsulation, growth, and division. *Science* 302:618–622.
6. Reeves JP, Dowben RM (1969) Formation and properties of thin-walled phospholipid vesicles. *J Cell Physiol* 73:49–60.
7. Olson F, Hunt CA, Szoka FC, Vail WJ, Papahadjopoulos D (1979) Preparation of liposomes of defined size distribution by extrusion through polycarbonate membranes. *Biochim Biophys Acta* 557:9–23.
8. Angelova MI, Dimitrov DS (1986) Liposome electroformation. *Faraday Discuss* 81:303–311.
9. Karlsson M, *et al.* (2000) Electroinjection of colloid particles and biopolymers into single unilamellar liposomes and cells for bioanalytical applications. *Anal Chem* 72:5857–5862.
10. Szoka F, Papahadjopoulos D (1978) Procedure for preparation of liposomes with large internal aqueous space and high capture by reverse-phase evaporation. *Proc Natl Acad Sci USA* 75:4194–4198.

BIOPHYSICS

11. Pautot S, Frisken BJ, Weitz DA (2003) Engineering asymmetric vesicles. *Proc Natl Acad Sci USA* 100:10718–10721.
12. Liu AP, Fletcher DA (2006) Actin polymerization serves as a membrane domain switch in model lipid bilayers. *Biophys J* 91:4064–4070.
13. Miyata H, Nishiyama S, Akashi K-i, Kinosita K, Jr (1999) Protrusive growth from giant liposomes driven by actin polymerization. *Proc Natl Acad Sci USA* 96:2048–2053.
14. Bucher P, Fischer A, Luisi PL, Oberholzer T, Walde P (1998) Giant vesicles as biochemical compartments: The use of microinjection techniques. *Langmuir* 14:2712–2721.
15. Colletier JP, Chaize B, Winterhalter M, Fournier D (2002) Protein encapsulation in liposomes: Efficiency depends on interactions between protein and phospholipid bilayer. *BMC Biotechnol* 2:9.
16. Pautot S, Frisken BJ, Weitz DA (2003) Production of unilamellar vesicles using an inverted emulsion. *Langmuir* 19:2870–2879.
17. Atencia J, Beebe DJ (2005) Controlled microfluidic interfaces. *Nature* 437:648–655.
18. Utada AS, *et al.* (2005) Monodisperse double emulsions generated from a microcapillary device. *Science* 308:537–541.
19. Gunther A, Jensen KF (2006) Multiphase microfluidics: From flow characteristics to chemical and materials synthesis. *Lab Chip* 6:1487–1503.
20. Funakoshi K, Suzuki H, Takeuchi S (2007) Formation of giant lipid vesicle-like compartments from a planar lipid membrane by a pulsed jet flow. *J Am Chem Soc* 129:12608–12609.
21. Funakoshi K, Suzuki H, Takeuchi S (2006) Lipid bilayer formation by contacting monolayers in a microfluidic device for membrane protein analysis. *Anal Chem* 78:8169–8174.
22. Maxworthy T (1972) Structure and stability of vortex rings. *J Fluid Mech* 51:15–32.
23. Dabiri JO, Gharib M (2004) Fluid entrainment by isolated vortex rings. *J Fluid Mech* 511:311–331.
24. Gharib M, Rambod E, Shariff K (1998) A universal time scale for vortex ring formation. *J Fluid Mech* 360:121–140.
25. Shusser M, Gharib M (2000) Energy and velocity of a forming vortex ring. *Phys Fluids* 12:618–621.
26. Saffman PG (1970) Velocity of viscous vortex rings. *Stud Appl Math* 49:371–380.
27. Shariff K, Leonard A (1992) Vortex rings. *Annu Rev Fluid Mech* 24:235–279.
28. Bar-Ziv R, Moses E, Nelson P (1998) Dynamic excitations in membranes induced by optical tweezers. *Biophys J* 75:294–320.
29. Rossier O, *et al.* (2003) Giant vesicles under flows: Extrusion and retraction of tubes. *Langmuir* 19:575–584.
30. Anno JN (1977) *The Mechanics of Liquid Jets* (Lexington Books, Lexington, MA).
31. Powers TR, Huber G, Goldstein RE (2002) Fluid-membrane tethers: Minimal surfaces and elastic boundary layers. *Phys Rev E* 65:041901.
32. Hope MJ, Bally MB, Webb G, Cullis PR (1985) Production of large unilamellar vesicles by a rapid extrusion procedure—Characterization of size distribution, trapped volume and ability to maintain a membrane-potential. *Biochim Biophys Acta* 812:55–65.
33. Holden MA, Needham D, Bayley H (2007) Functional bionetworks from nanoliter water droplets. *J Am Chem Soc* 129:8650–8655.
34. Suzuki H, Tabata KV, Noji H, Takeuchi S (2006) Highly reproducible method of planar lipid bilayer reconstitution in polymethyl methacrylate microfluidic chip. *Langmuir* 22:1937–1942.
35. Stachowiak JC, *et al.* (2007) Piezoelectric control of needle-free transdermal drug delivery. *J Controlled Release* 124:89–97.